

Gaze into the Details: Locality-Sensitive Enhancement for OCTA Retinal Vessel Segmentation

Tuopusen Huang, Ding Ma, Xiangqian Wu *
 Faculty of Computing
 Harbin Institute of Technology
 Harbin, China

tuopusen.huang@stu.hit.edu.cn, madingcs@hit.edu.cn, xqwu@hit.edu.cn

Abstract

Existing deep learning frameworks for Optical Coherence Tomography Angiography (OCTA) vessel segmentation are largely derived from the U-Net architecture, which serves as the foundation for most current designs. However, most of these methods focus only on holistic representation, struggling to address the problem of low local contrast unique to OCTA, which leads to vessel discontinuities and loss of detail. To address these problems, we propose LSENet, which builds upon the U-Net architecture by introducing three core innovative modules: To address vessel discontinuities, we introduce the Patch Information Enhance module (PIE), which replaces standard skip connections to execute patch-wise attention. To mitigate detail loss, the Multiscale Feature Fusion module (MFF) is proposed to feed the PIE module rich, multi-scale information by extracting visually interpretable features from both the original input and preceding layers. Finally, the Connectivity Refinement Decoder (CRD) is designed to refine features from all levels and utilize a large kernel in the final convolutional layer to reduce fragmentation. Experiments on three public datasets (OCTA-500, ROSE-1, and ROSSA) demonstrate that our proposed LSENet achieves state-of-the-art performance while requiring fewer parameters.

1. Introduction

Optical Coherence Tomography Angiography (OCTA) is a non-invasive imaging technique for high-resolution visualization of the ocular microvasculature [3, 12, 34, 37], which holds significant value in the diagnosis and monitoring of pathologies such as diabetic retinopathy, macular degeneration, and glaucoma [25, 29, 36]. Artificial Intelligence and Deep Learning are increasingly utilized to enable the automated and reproducible analysis of OCTA data, thereby

*corresponding author.

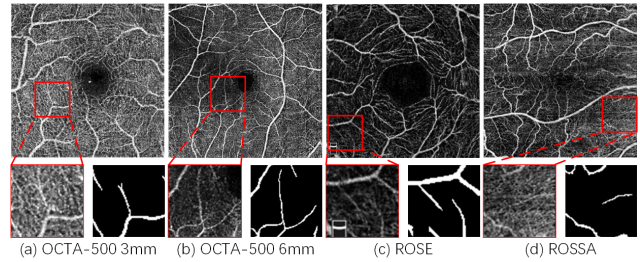


Figure 1. Examples of low local contrast challenges from the OCTA-500, ROSE-1, and ROSSA datasets. (a) illustrates low contrast in a bright region, while (b)-(d) show low contrast in dark regions. In all subfigures, the magnified local region (bottom left) shows vessels that are difficult to distinguish from the background, as confirmed by the ground truth (bottom right), posing a segmentation challenge.

improving screening, diagnosis, and treatment monitoring [15]. However, achieving accurate retinal vessel segmentation faces multiple challenges [14]: The low image Signal-to-Noise Ratio, coupled with the complex structure, diverse orientations, varied sizes of the retinal vasculature, and low local contrast make segmentation extremely difficult. Furthermore, the low local contrast leads to ambiguity in uncertain regions, such as microvessels, vessel edges, and endpoints, resulting in vessel discontinuities and loss of detail.

In recent years, numerous deep learning studies have been proposed for retinal vessel segmentation in OCTA images to address the field’s inherent challenges. **Customized U-Net architectures** [18, 40] refine the standard U-Net structure to enhance vessel recognition specifically for the OCTA modality. **Transformer-based architectures** [21, 38, 41] employ token-based processing, tokenizing vessel semantics to effectively capture global contextual information. Additionally, **specialized strategies for data optimization and label scarcity** [22, 27] leverage specific training protocols or network designs to enhance the model’s information capture capabilities.

Concurrently, most methods rely on holistic representa-

tion, effectively taking a “glance” at global features. While this approach excels at capturing the geometry of main vessels and preserving global spatial context, it struggles with the prevalent challenge of low local contrast in OCTA data (as shown in Fig. 1), especially at the distal ends of target vessels. Consequently, models relying on these holistic features often fail to segment the fine vascular endings accurately, leading to vessel discontinuities and a loss of detail. To address these limitations, we posit that processing these local regions individually, free from the interference of the global foreground and background, enables a more robust identification of these low contrast regions. Accordingly, we propose LSENet, a lightweight and efficient network that builds upon the holistic “glance” of its U-Net architecture by augmenting it with a locality-sensitive, patch-based module, enabling it to “gaze into details” by amplifying multi-scale feature information within localized regions.

Specifically, we strengthen the global features derived from the primary U-Net by incorporating local perception capabilities through three core modules. We propose a Patch Information Enhance module (PIE) that, instead of operating directly on global features, partitions the feature map into several patches. This allows the model to focus on extracting regions containing vessel information individually within each local patch. Furthermore, we introduce a Multiscale Feature Fusion module (MFF) to decompose the global features at multiple scales before they are fed into the PIE module. The MFF is designed to extract vessel features at various scales, subsequently fusing and selecting the most salient feature information, thereby supplying PIE with enhanced potential vascular details. While this additional vascular information helps the PIE module identify hard-to-detect, low-contrast target vessels, it may also introduce more false positives (refer to Sec. 4.4). To mitigate this risk, we propose a Connectivity Refinement Decoder (CRD) that utilizes a large kernel convolution as the final output layer to ensure the model achieves higher vessel connectivity.

The contributions of our study are summarized as follows:

- We propose a novel Locality-Sensitive Enhancement Network (LSENet), which employs a patch-based processing methodology to “gaze into details” in OCTA vessel segmentation. To our knowledge, this network is the first in the OCTA vessel segmentation domain to leverage a locality-sensitive information enhancement strategy.
- We introduce three core modules that enable the model to emphasize vascular details: The MFF module extracts and fuses multi-scale features to overcome detail loss; the PIE module assigns patch-wise attention to handle vessel discontinuities; and the CRD uses a large convolution kernel on the refined information to ensure superior connectivity.
- We demonstrate the state-of-the-art performance of our method on the OCTA vessel segmentation task through extensive experiments on three publicly available datasets (ROSE-1 [24], OCTA-500 [17], and ROSSA [27]).

2. Related Works

2.1. Retina Vessel Segmentation

Retina vessel segmentation, historically focused on Color Fundus Photography (CFP), was long dominated by the U-Net architecture [33]. This framework was progressively refined with enhanced context, attention, and boundary modeling [6, 8, 26, 46]; adaptations for complex morphology via deformable convolutions and multi-scale interaction [11, 20, 42, 44, 45]; and more efficient architecture [43].

These foundational studies informed subsequent work on OCTA, which has emerged as a mainstream retinal vessel examination method owing to its high-resolution, 3D microvascular details [3, 12, 34, 37]. However, these advanced characteristics also introduce novel challenges to vessel segmentation, such as intricate structures and low local contrast, rendering methodologies from previous modalities suboptimal. Consequently, OCTA-specific methods have been developed, including: **customized U-Net architectures** that employ dual-branch designs, directional convolutions, or multi-task learning [1, 9, 18, 40]; **Transformer architectures** [39] that leverage hybrid CNN-Transformer models or adapted foundation models [21, 38, 41]; and **strategies targeting data optimization** through multi-modal fusion, 3D-to-2D projection, and semi-supervised or unsupervised approaches [13, 16, 22, 27, 30, 35].

2.2. Local Enhancement Methods

Strategies for local enhancement, wherein an image is partitioned into patches or regions to extract fine-grained details, represent a pivotal research area in both natural and medical image processing.

In the natural image domain, this paradigm is applied across diverse tasks. For image classification, ViT [5] partitions images into patch-based tokens. For semantic segmentation, the Swin Transformer [23] computes self-attention within hierarchical shifted windows”. For object detection, the Twins model [4] combines Locally-grouped (LSA) and Global Sub-sampled (GSA) attention. For facial recognition, PACVT [19] employs a Patch Attention Unit” (PAU), and for image captioning, the Patch Matters model [28] uses a divide-then-aggregate” strategy. Additionally, local feature enhancement is critical for processing sparse spatio-temporal signals [31, 32]. **In the medical imaging domain**, this methodology is widely adopted for localized pathology analysis. For organ segmentation, Swin-Unet [2] adapts the Swin Transformer’s shifted window” mech-

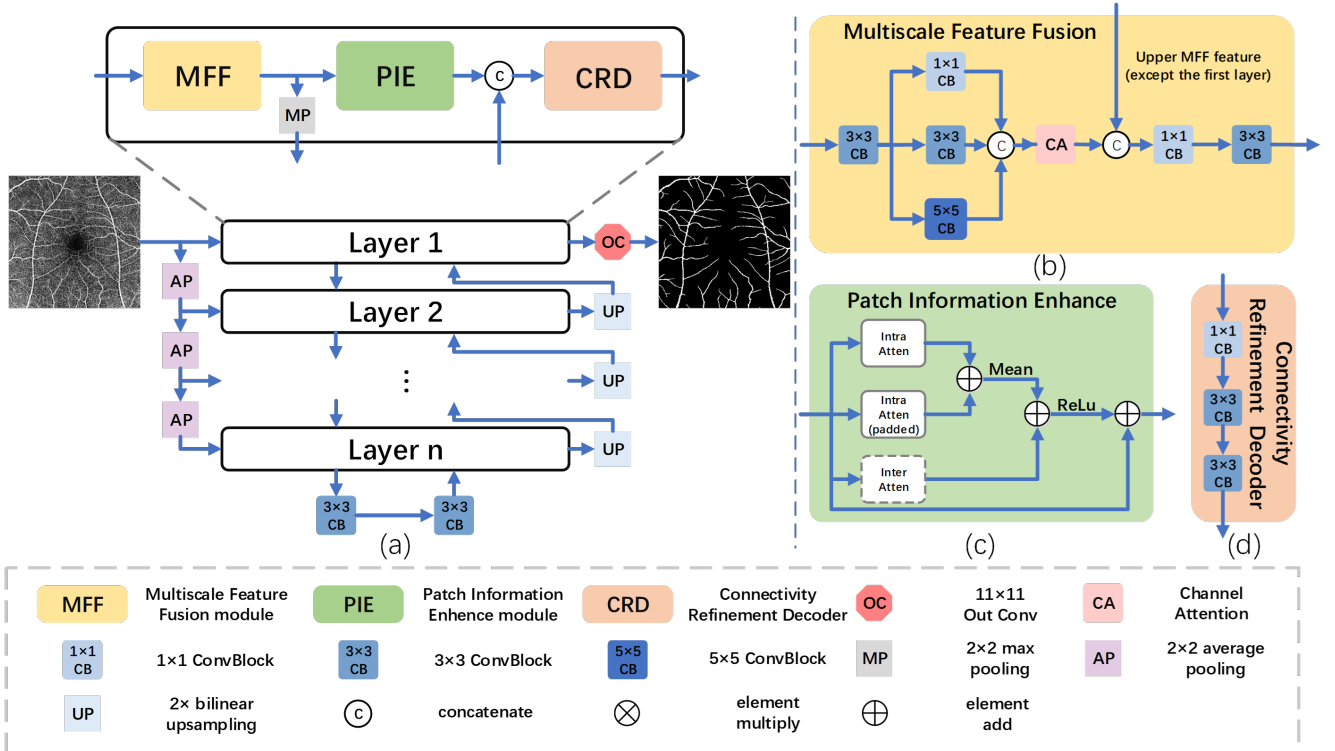


Figure 2. Architecture of LSENet and its core modules. (a) The main architecture, composed of stacked layers (each with three modules). (b) Multiscale Feature Fusion (MFF) module: Fuses vessel features using multiscale kernels and channel attention. (c) Patch Information Enhance (PIE) module: Handles vessel discontinuities via intra- and inter-patch attention. (d) Connectivity Refinement Decoder (CRD): Refines layer-wise features and, aided by a final large-kernel convolution, maintains vessel connectivity.

anism. For Alzheimer’s disease diagnosis, DA-MIDL [47] utilizes Patch-Nets” with spatial attention. For breast tumor classification, SGLA-Net [10] integrates global and local representations via a Global-Local Feature Interaction” (GLFI) block. For melanoma analysis, GPLE [48] introduces a “Supplement Shifted Window Partition” (SSWP).

Despite the widespread adoption of these local enhancement strategies in other domains, to the best of our knowledge, this paradigm has not yet been applied to the specific task of vessel segmentation within the OCTA domain. Our work, therefore, aims to address this research gap.

3. Methodology

3.1. Overall Framework

We propose the Locality-Sensitive Enhancement Network (LSENet) to address the challenges posed by low local contrast in OCTA images. As shown in Fig. 2, the LSENet architecture is built on a lightweight U-Net backbone, modified with a constant 64-channel count to reduce parameters.

Our core contributions are three modules that replace U-Net components: the **Multiscale Feature Fusion module (MFF)**, which extracts rich, multi-scale features from the raw input at various resolutions; the **Patch Information Enhance module (PIE)**, which replaces standard skip con-

nections and employs patch-based processing to perform targeted local information enhancement in challenging regions; and the **Connectivity Refinement Decoder (CRD)**, a lightweight decoder that refines features from the PIE module and upsampling path, cooperating with a final large-kernel convolution to ensure vessel connectivity.

3.2. Patch Information Enhance Module (PIE)

To explicitly capture local context while avoiding global extreme values, PIE (Fig. 2) replaces standard skip connections with a dual-branch patch-wise attention mechanism:

Intra-Patch Attention (Fig. 3 a): Given an input $X \in \mathbb{R}^{C \times H \times W}$, we symmetrically pad it to be divisible by patch size P . Query (Q_{intra}), Key (K_{intra}), and Value (V_{intra}) are generated via convolutions (5×5 for Q_{intra}, K_{intra} to capture spatial priors; 1×1 for V_{intra}) and subsequently reshaped into non-overlapping patches of shape $\mathbb{R}^{N \times C \times P^2}$, where $N = \frac{H}{P} \times \frac{W}{P}$. By treating the P^2 pixels as the sequence length, attention is computed independently within each patch using a relative position encoding P_{pos} :

$$\text{Attn}_{intra} = \text{Attn}(Q_{intra}, K_{intra}, V_{intra}) \quad (1)$$

$$\text{Attn}(Q, K, V) = \text{Softmax} \left(\frac{QK^T + P_{pos}}{\sqrt{C}} \right) V \quad (2)$$

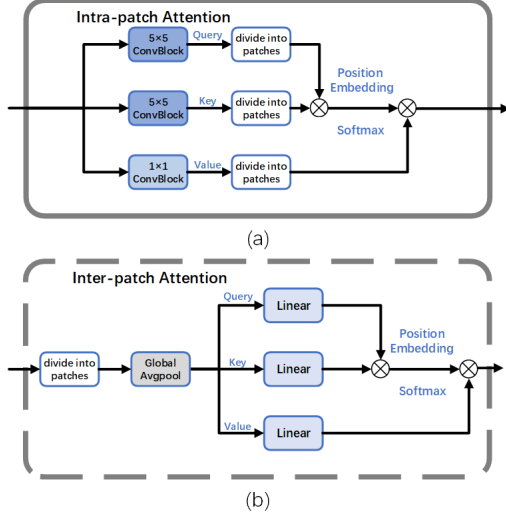


Figure 3. Components of the PIE module. (a) Intra-patch Attention: Enhances vessel features within patches. (b) Inter-patch Attention: Compensates for global information loss between patches.

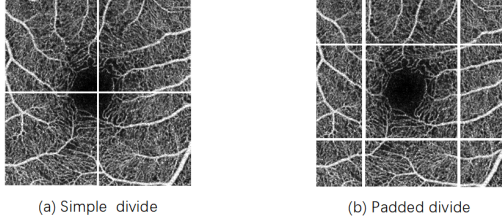


Figure 4. Interleaved partitioning for PIE intra-patch attention, illustrating (a) the simple (non-shifted) grid and (b) the shifted (padded) grid. Combining these overlapping strategies mitigates the limitations of a single partition, enhancing segmentation robustness. (Note: Patches enlarged for clarity).

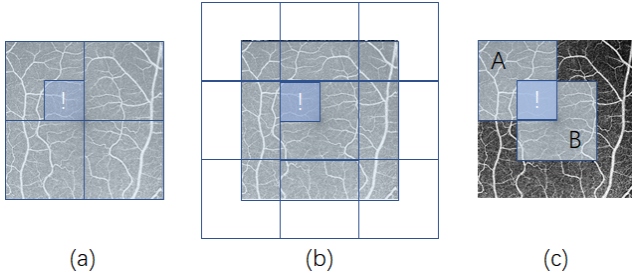


Figure 5. Receptive field comparison. (a) Original partitioning. (b) Shifted partitioning (padded by $P/2$). (c) The combined strategy doubles the effective receptive field.

Shifted Intra-Patch Attention: To prevent continuous vessels from being artificially severed by fixed boundaries, a parallel branch applies the identical $\text{Patch}(\cdot)$ and attention operations to X after padding it by $P/2$ on all sides. The output is then cropped back to its original size ($\text{Attn}_{\text{intra, padding}}$). This shifted window approach enables cross-patch information flow, doubling the effective receptive field (Fig. 5).

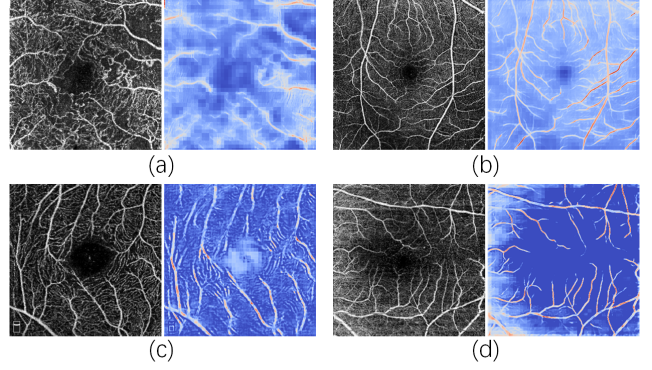


Figure 6. Attention heatmaps demonstrating PIE's focus. High attention (red) strongly aligns with target vessels compared to the background (blue).

Inter-Patch Attention (Fig. 3 b): To recapture necessary global context, we apply spatial average pooling to each patch, yielding N tokens. Linear layers generate Q, K, V , and standard attention is computed across the N patches. The output ($\text{Attn}_{\text{inter}}$) is reshaped and bilinearly interpolated back to $H \times W$.

The final feature X_{PIE} fuses the three branches, followed by a ReLU activation and a residual connection:

$$\text{Attn}_X = \frac{\text{Attn}_{\text{intra}} + \text{Attn}_{\text{intra, padding}} + \text{Attn}_{\text{inter}}}{2} \quad (3)$$

$$X_{PIE} = \text{ReLU}(\text{Attn}_X) + X \quad (4)$$

As validated in Fig. 6, the module's attention heatmaps confirm that PIE functions as an effective local enhancer, providing refined, discriminative vessel features for the decoder.

3.3. Multiscale Feature Fusion Module (MFF)

The MFF module (Fig. 2) is designed to feed rich, interpretable features to the PIE module. It takes two inputs: X_{down} (the output from the previous MFF layer) and X_{in} (the raw input image downsampled via average pooling).

The X_{in} input first passes through a 3×3 convolution block (X_{pre} , Eq. 5), followed by parallel 1×1 , 3×3 , and 5×5 convolution blocks to extract multi-scale features (Eqs. 6). In $X_{n \times n}$, $n \times n$ denotes the size of the convolution kernel. Specifically, the convolution block (ConvBlock) includes one convolution, one GroupNorm, and one ReLU.

$$X_{\text{pre}} = \text{ConvBlock}_{3 \times 3}(X_{\text{in}}) \quad (5)$$

$$X_{n \times n} = \text{ConvBlock}_{n \times n}(X_{\text{pre}}) \quad (6)$$

These features (X_{multi}) are screened by a Channel Attention (CA) [26] module (X_{att} , Eqs. 7-8). X_{att} is then concatenated with X_{down} (Eq. 9) and fused via a 1×1 conv (Eq. 10) and a 3×3 conv (Eq. 11) to produce the final 64-channel output.

$$X_{\text{multi}} = \text{Concat}(X_{1 \times 1}, X_{3 \times 3}, X_{5 \times 5}) \quad (7)$$

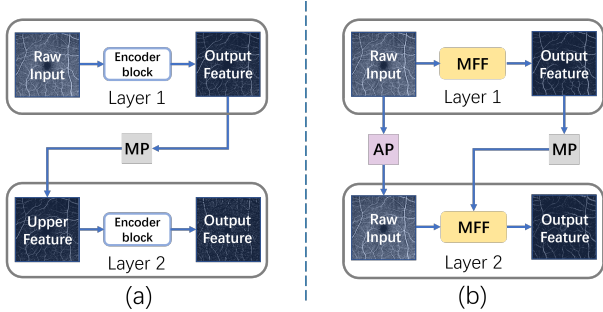


Figure 7. Input strategy comparison. (a) A standard U-Net block receives only max-pooled features from the preceding layer. (b) Our MFF module additionally receives the average-pooled raw input, a design that preserves visual interpretability at each stage.

$$X_{att} = CA(X_{multi}) \quad (8)$$

$$X_{concat} = \text{Concat}(X_{att}, X_{down}) \quad (9)$$

$$X_{fusion} = \text{ConvBlock}_{1 \times 1}(X_{concat}) \quad (10)$$

$$X_{MFF} = \text{ConvBlock}_{3 \times 3}(X_{fusion}) \quad (11)$$

Critically, to ensure our PIE module operates on meaningful local structures while maintaining visual interpretability, we use the downsampled raw image X_{in} as the primary input, rather than only the abstract features from former encoder layers (Fig. 7).

Furthermore, to ensure robustness to the small batch sizes prevalent in medical imaging, all convolutional blocks in our network employ GroupNorm (8 channels/group) instead of BatchNorm.

3.4. Connectivity Refinement Decoder (CRD)

Our Connectivity Refinement Decoder (CRD) (Fig. 2) is a lightweight component designed to maintain a 64-channel output. At each stage, its core function is to refine up-sampled features X_{up} by fusing them with incoming PIE features X_{PIE} using a 1×1 convolution block (Eq. 12). This intermediate representation, X_{refine} , is then processed through two consecutive 3×3 convolution blocks to produce the stage’s output, X_{CRD} (Eq. 13).

$$X_{refine} = \text{ConvBlock}_{1 \times 1}(\text{Concat}(X_{up}, X_{PIE})) \quad (12)$$

$$X_{CRD} = \text{ConvBlock}_{3 \times 3}(\text{ConvBlock}_{3 \times 3}(X_{refine})) \quad (13)$$

The most critical component is the final output layer. We replace the standard 1×1 ‘OutConv’ with a large 11×11 no bias convolution (Fig. 8). This is motivated by the continuous nature of vessels; segmenting a pixel requires contextual information from a larger neighborhood. While this introduces minor border artifacts, experiments (Sec. 4.4) confirm it significantly improves vessel connectivity and reduces fragmented endpoints.

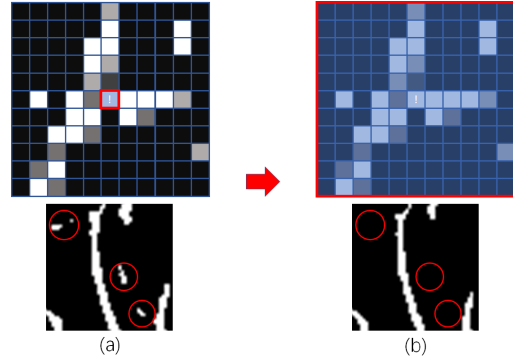


Figure 8. Improved Output Convolution (OutConv) comparison. (a) A standard U-Net’s 1×1 kernel has a receptive field limited to a single point. (b) LSENet’s 11×11 large kernel captures broader vascular context, significantly improving vessel connectivity and reducing isolated false positives.

3.5. Loss function

We employ a combined loss function, $Loss = Loss_{bce} + Loss_{dice}$, where the Binary Cross-Entropy (BCE) Loss (Eq. 14) guides the model in learning the overall vessel distribution (particularly during early training), while the DiceLoss (Eq. 15) focuses on optimizing the fine-grained segmentation of vessel details and endpoints.

$$Loss_{bce} = -\frac{1}{n} \sum_{i=1}^n [y_i \log(\hat{y}_i) + (1 - y_i) \log(1 - \hat{y}_i)] \quad (14)$$

$$Loss_{dice} = 1 - \frac{2 \sum_{i=1}^n y_i \hat{y}_i}{\sum_{i=1}^n y_i + \sum_{i=1}^n \hat{y}_i} \quad (15)$$

Here, \hat{y}_i is the i -th pixel’s predicted value, and y_i is its ground truth label.

4. Experiments

4.1. Datasets and Metrics

We evaluate our model on three public OCTA vessel segmentation datasets: ROSE-1 [24], OCTA-500 [17], and ROSSA [27]. **ROSE-1** [24]: Contains 39 images (304×304 , 3×3 mm²) of the Superficial Vascular Complex (SVC). We follow the official split (27 Train / 3 Val / 9 Test). **OCTA-500** [17]: Includes two subsets: OCTA-6M (6×6 mm²) and OCTA-3M (3×3 mm²). We use the large-vessel annotations from the ILM-OPL maximum projection and follow the official splits: 240/10/50 (Train/Val/Test) for OCTA-6M and 140/10/50 for OCTA-3M. **ROSSA** [27]: We use the 300 manually annotated images, splitting them into 240/10/50 (Train/Val/Test) following the previous ratio.

We utilize six standard metrics to comprehensively evaluate the model’s performance from different perspectives: **Dice**: The primary metric for evaluating spatial overlap between the prediction and ground truth, especially suitable for imbalanced tasks like vessel segmentation. **Sensitivity**

Table 1. Quantitative comparison results for retinal vessel segmentation on the OCTA-500, ROSE-1 and ROSSA datasets (Mean \pm SD). **Bold** indicates the best performance, underline indicates the second best, and double underline indicates the third best. “ \uparrow ” means the higher the better, while “ \downarrow ” means the lower the better.

Dataset	Model	Venue(year)	Dice% \uparrow	Sensitivity% \uparrow	Specificity% \uparrow	FDR% \downarrow	Accuracy% \uparrow	Kappa% \uparrow
OCTA-500 3mm	UNet	MICCAI(2015)	91.02 \pm 0.06	90.30 \pm 0.94	<u>99.41 \pm 0.08</u>	<u>8.23 \pm 0.92</u>	98.80 \pm 0.01	90.38 \pm 0.07
	CENet	TMI(2019)	89.33 \pm 0.05	89.31 \pm 0.37	99.23 \pm 0.03	10.65 \pm 0.31	98.56 \pm 0.01	88.55 \pm 0.05
	VesselNet	MICCAI(2019)	90.20 \pm 0.06	89.01 \pm 0.15	99.40 \pm 0.01	8.58 \pm 0.10	98.69 \pm 0.01	89.50 \pm 0.07
	CSNet	MedIA(2021)	91.11 \pm 0.05	<u>90.92 \pm 0.56</u>	99.37 \pm 0.05	8.69 \pm 0.58	98.80 \pm 0.01	90.47 \pm 0.05
	UTNet	MICCAI(2021)	<u>91.32 \pm 0.22</u>	91.37 \pm 0.75	99.37 \pm 0.05	8.72 \pm 0.58	<u>98.83 \pm 0.03</u>	<u>90.69 \pm 0.23</u>
	SwinUNet	ECCV(2022)	88.37 \pm 0.04	88.02 \pm 0.28	99.19 \pm 0.02	11.27 \pm 0.26	<u>98.44 \pm 0.01</u>	87.53 \pm 0.05
	OCT2Former	CMPB(2023)	90.51 \pm 0.24	89.14 \pm 0.92	<u>99.43 \pm 0.05</u>	<u>8.06 \pm 0.60</u>	98.74 \pm 0.02	89.84 \pm 0.25
	FRNet	ICASSP(2024)	90.80 \pm 0.09	90.61 \pm 0.55	99.35 \pm 0.05	9.01 \pm 0.57	98.76 \pm 0.02	90.13 \pm 0.10
	DGNet	BSPC(2025)	<u>91.26 \pm 0.05</u>	90.86 \pm 0.49	99.40 \pm 0.04	8.33 \pm 0.45	<u>98.83 \pm 0.01</u>	<u>90.63 \pm 0.06</u>
	LSENet(Ours)			92.03 \pm 0.11	<u>91.25 \pm 0.61</u>	99.49 \pm 0.05	7.17 \pm 0.62	98.93 \pm 0.02
OCTA-500 6mm	UNet	MICCAI(2015)	88.13 \pm 0.04	87.01 \pm 0.35	98.91 \pm 0.04	<u>10.73 \pm 0.35</u>	<u>97.78 \pm 0.01</u>	86.90 \pm 0.04
	CENet	TMI(2019)	87.38 \pm 0.04	88.28 \pm 0.34	98.56 \pm 0.05	13.51 \pm 0.34	<u>97.58 \pm 0.01</u>	86.04 \pm 0.04
	VesselNet	MICCAI(2019)	87.30 \pm 0.10	86.01 \pm 0.58	<u>98.85 \pm 0.07</u>	<u>11.36 \pm 0.56</u>	97.63 \pm 0.02	86.00 \pm 0.11
	CSNet	MedIA(2021)	<u>88.20 \pm 0.09</u>	<u>88.76 \pm 0.40</u>	98.69 \pm 0.07	12.35 \pm 0.50	97.75 \pm 0.03	86.96 \pm 0.10
	UTNet	MICCAI(2021)	<u>88.65 \pm 0.19</u>	<u>88.70 \pm 1.22</u>	98.81 \pm 0.17	11.38 \pm 1.29	<u>97.85 \pm 0.05</u>	<u>87.46 \pm 0.21</u>
	SwinUNet	ECCV(2022)	86.31 \pm 0.04	85.80 \pm 0.53	98.64 \pm 0.07	13.17 \pm 0.55	<u>97.42 \pm 0.02</u>	84.89 \pm 0.04
	OCT2Former	CMPB(2023)	87.40 \pm 0.27	86.96 \pm 0.54	98.74 \pm 0.12	12.14 \pm 0.93	97.63 \pm 0.07	86.09 \pm 0.30
	FRNet	ICASSP(2024)	87.59 \pm 0.14	<u>88.84 \pm 0.42</u>	98.53 \pm 0.07	13.63 \pm 0.55	97.62 \pm 0.04	86.27 \pm 0.16
	DGNet	BSPC(2025)	88.17 \pm 0.07	88.58 \pm 0.77	98.71 \pm 0.11	12.23 \pm 0.80	97.75 \pm 0.03	<u>86.92 \pm 0.08</u>
	LSENet(Ours)			89.14 \pm 0.06	88.88 \pm 0.52	98.90 \pm 0.08	10.59 \pm 0.59	97.95 \pm 0.02
ROSE-1	UNet	MICCAI(2015)	86.75 \pm 0.18	89.00 \pm 0.62	<u>97.41 \pm 0.20</u>	<u>15.39 \pm 0.89</u>	96.25 \pm 0.08	84.56 \pm 0.23
	CENet	TMI(2019)	82.27 \pm 0.12	84.41 \pm 0.21	96.68 \pm 0.09	19.76 \pm 0.37	94.98 \pm 0.05	79.35 \pm 0.15
	VesselNet	MICCAI(2019)	84.52 \pm 0.13	85.53 \pm 0.51	97.30 \pm 0.10	16.47 \pm 0.43	95.68 \pm 0.04	82.01 \pm 0.15
	CSNet	MedIA(2021)	86.63 \pm 0.26	90.21 \pm 0.33	97.11 \pm 0.14	16.68 \pm 0.62	96.16 \pm 0.09	84.39 \pm 0.31
	UTNet	MICCAI(2021)	<u>86.97 \pm 0.19</u>	90.03 \pm 0.84	97.28 \pm 0.19	15.88 \pm 0.83	<u>96.28 \pm 0.07</u>	<u>84.80 \pm 0.23</u>
	SwinUNet	ECCV(2022)	78.28 \pm 0.06	80.35 \pm 0.26	96.01 \pm 0.06	23.69 \pm 0.24	93.85 \pm 0.03	74.70 \pm 0.07
	OCT2Former	CMPB(2023)	<u>87.78 \pm 0.12</u>	<u>90.31 \pm 0.62</u>	<u>97.53 \pm 0.17</u>	<u>14.61 \pm 0.75</u>	<u>96.53 \pm 0.06</u>	<u>85.76 \pm 0.16</u>
	FRNet	ICASSP(2024)	85.86 \pm 0.35	<u>90.29 \pm 0.83</u>	96.79 \pm 0.31	18.14 \pm 1.31	95.90 \pm 0.16	83.47 \pm 0.45
	DGNet	BSPC(2025)	86.67 \pm 0.17	91.42 \pm 0.46	96.88 \pm 0.16	17.60 \pm 0.67	96.12 \pm 0.08	84.41 \pm 0.22
	LSENet(Ours)			88.22 \pm 0.07	89.85 \pm 0.80	97.79 \pm 0.17	13.34 \pm 0.82	96.69 \pm 0.04
ROSSA	UNet	MICCAI(2015)	<u>90.60 \pm 0.20</u>	89.34 \pm 0.67	99.09 \pm 0.05	<u>8.09 \pm 0.34</u>	<u>98.08 \pm 0.03</u>	<u>89.54 \pm 0.22</u>
	CENet	TMI(2019)	89.10 \pm 0.04	89.14 \pm 0.37	98.74 \pm 0.06	10.94 \pm 0.44	<u>97.75 \pm 0.02</u>	<u>87.84 \pm 0.05</u>
	VesselNet	MICCAI(2019)	89.34 \pm 0.14	87.49 \pm 0.40	99.04 \pm 0.05	8.72 \pm 0.40	97.84 \pm 0.03	88.14 \pm 0.15
	CSNet	MedIA(2021)	90.04 \pm 0.22	<u>90.11 \pm 0.56</u>	98.84 \pm 0.10	10.04 \pm 0.73	97.94 \pm 0.05	88.89 \pm 0.25
	UTNet	MICCAI(2021)	<u>91.33 \pm 0.17</u>	<u>90.60 \pm 0.67</u>	<u>99.10 \pm 0.09</u>	<u>7.93 \pm 0.72</u>	<u>98.22 \pm 0.04</u>	<u>90.33 \pm 0.19</u>
	SwinUNet	ECCV(2022)	87.84 \pm 0.05	87.44 \pm 0.38	98.66 \pm 0.06	11.76 \pm 0.43	97.50 \pm 0.02	86.44 \pm 0.06
	OCT2Former	CMPB(2023)	89.54 \pm 0.15	87.39 \pm 0.97	<u>99.10 \pm 0.10</u>	8.19 \pm 0.76	97.89 \pm 0.01	88.37 \pm 0.15
	FRNet	ICASSP(2024)	89.80 \pm 0.15	89.35 \pm 0.49	<u>98.89 \pm 0.09</u>	9.73 \pm 0.65	97.90 \pm 0.04	88.63 \pm 0.17
	DGNet	BSPC(2025)	90.27 \pm 0.19	89.43 \pm 0.78	99.00 \pm 0.09	8.87 \pm 0.68	98.01 \pm 0.04	89.16 \pm 0.21
	LSENet(Ours)			91.59 \pm 0.15	90.89 \pm 0.51	99.13 \pm 0.08	7.69 \pm 0.62	98.27 \pm 0.04

(Sen): Measures the ability to correctly identify actual vessels. High Sen indicates a higher target vessel recognition rate. **Specificity (Spe)**: Measures the ability to correctly identify the background. High Spe indicates good noise suppression and few false alarms. **Accuracy (Acc)**: The overall correct classification rate for all pixels. **False Discovery Rate (FDR)**: Measures the proportion of incorrect predictions among all pixels predicted as vessels. Low FDR represents high precision. **Kappa Coefficient (Kappa)**: A robust metric for agreement that corrects for the possibility of chance agreement. The evaluation dimensions of these six metrics are distinct and complementary.

4.2. Implementation Details

All models were trained using an Intel(R) Xeon(R) Gold 6226R CPU and an NVIDIA RTX 3090 GPU for 500 epochs (batch size=2) using the Adam optimizer (LR=5e-4, weight decay=1e-4) with a polynomial LR decay (power=0.9) and early stopping (patience=100). To pre-

vent overfitting, we applied aggressive data augmentation (random horizontal/vertical flips, $\pm 30^\circ$ rotations). The total layer number was set to 4, with a patch size of 20 for the OCTA-500 6mm dataset and 15 for the remaining three.

4.3. Comparative Analysis

We compare LSENet against nine SOTA methods: U-Net [33], CS-Net [26], CE-Net [8], SwinUNet [2], DGNet [18], FRNet [27], Vessel-Net [43], UTNet [7], and OCT2former [38]. All models were trained in the same training environment, using the learning rates, loss functions, and optimizers from their respective papers to ensure a fair comparison. We present the mean and standard deviation of the metrics after five consecutive training runs.

Tab. 1 shows the quantitative results. **Overall**, our proposed LSENet achieves SOTA performance, ranking first on the vast majority of metrics across all three datasets. The high Dice, FDR, and Kappa metrics indicate that our model can identify target vessels more accurately and reliably, re-

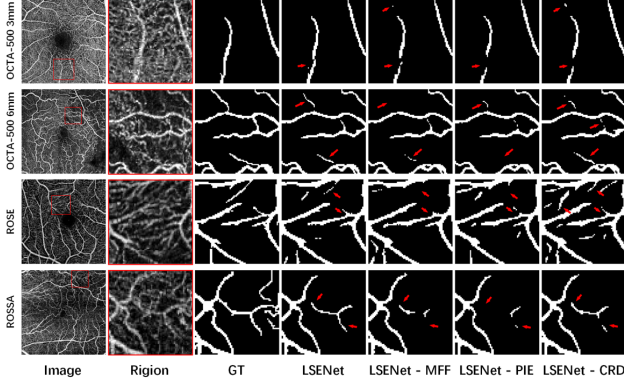


Figure 9. Qualitative results of the ablation study for each module. From top to bottom, each row corresponds to one sample from OCTA-500 3mm, OCTA-500 6mm, ROSE-1, and ROSSA, respectively. Removing MFF, PIE, or CRD leads to distinct failure modes (loss of detail, fragmentation, and poor connectivity).

ducing the occurrence of false positives. While it does not top every metric, the exceptions are typically in Sensitivity (Sen) or Specificity (Spe). This is expected, as these two metrics represent a trade-off: a model aggressively optimized to capture every faint vessel (high Sen) may inadvertently increase false positives (lower Spe), and vice versa.

OCTA-500 3mm: This dataset serves as a standard baseline, featuring a moderate sample size and a balanced segmentation difficulty. On the 3mm dataset, our method performed the best on all metrics except Sen. The Dice, FDR, and Kappa metrics reached 92.03% , 7.17% , and 91.45% , respectively, significantly surpassing the second-place method by 0.71% , 0.89% , and 0.76% .

OCTA-500 6mm: While larger in sample size, this dataset presents a greater challenge due to its wider imaging area, which includes a higher density of segmentation targets and more complex structures. On the 6mm dataset, our method demonstrated top-tier performance by ranking first on all metrics except for Spe. This lead was particularly significant in Dice and Kappa, where our model outperformed the second-place method by 0.49% and 0.55% , respectively.

ROSE-1: This dataset is significantly smaller, which rigorously tests the model’s learning efficiency and its ability to generalize from limited data. On this dataset, our model also achieved the best performance. Apart from the Sen metric, it surpassed the second-place OCT2Former by substantial margins in key metrics, leading in FDR by 1.27% , Kappa by 0.54% , and Dice by 0.44% .

ROSSA: As a recent dataset, ROSSA is characterized by a higher prevalence of noise, directly challenging the model’s noise suppression capabilities and overall robustness. Through the collaboration of the three modules, our model demonstrated superior performance by achieving the best results across all metrics, securing the top rank and establishing a state-of-the-art over the second-place UTNet.

Table 2. Ablation study of the Multiscale Feature Fusion module (MFF), Patch Information Enhance module (PIE), and Connectivity Refinement Decoder (CRD) on the OCTA-500 6mm dataset. (Mean \pm SD). The formatting and symbol conventions are the same as those defined in Tab. 1.

MFF	PIE	CRD	Dice% \uparrow	Sen% \uparrow	Spe% \uparrow	FDR% \downarrow	Acc% \uparrow	Kappa% \uparrow
×	×	×	88.49	88.72	98.77	11.73	97.81	87.28
×	✓	×	88.81	88.73	<u>98.84</u>	<u>11.10</u>	97.88	87.64
✓	×	×	88.89	<u>89.22</u>	98.79	11.43	97.89	87.72
×	×	✓	88.85	89.15	98.80	11.43	97.88	87.68
✓	×	✓	<u>89.01</u>	88.62	98.90	10.60	97.93	<u>87.86</u>
×	✓	✓	88.96	<u>89.38</u>	98.79	11.46	<u>97.90</u>	87.80
✓	✓	×	<u>88.98</u>	89.42	98.79	11.44	97.90	<u>87.82</u>
✓	✓	✓	89.14	88.88	<u>98.90</u>	10.59	97.95	88.01

4.4. Ablation Study

We conducted a thorough ablation study to validate the contribution of each proposed module. Tab. 2 presents the results of experiments performed on the OCTA-500 6mm dataset, selected for its larger data volume and greater segmentation difficulty. Starting from a baseline model (a U-Net with channels fixed at 64), the metrics quantitatively demonstrate the performance improvement provided by each individual module. Fig. 9 provides a qualitative visualization of the specific contribution of each proposed module. For a clear comparison, we illustrate the segmentation results of the full LSENet against variants where each module has been individually removed.

PIE (Patch Information Enhance module): This module focuses on regional feature selection. It selectively enhances features in challenging areas, such as low-contrast regions, while suppressing background noise. When PIE is removed, the model’s perceptual ability in these low-contrast areas drops sharply, manifesting as large segments of the target vasculature breaking or disappearing (Fig. 9 the second-to-last column).

MFF (Multiscale Feature Fusion module): This module enriches the feature representation. Without MFF, the model’s ability to perceive vessels at different scales noticeably degrades, leading to weakened identification of finer vessels (Fig. 9 the third-to-last column). While the inclusion of MFF might introduce more potential candidates by increasing sensitivity, it fundamentally enhances the model’s foundational perceptual capability.

CRD (Connectivity Refinement Decoder): This module acts as a refinement stage. Leveraging its large receptive field (11×11 kernel), it makes a more “cautious” and context-aware decision when producing the final output. Without CRD, the segmentation results become fragmented, connectivity decreases, and false positives increase (Fig. 9 the last column).

In summary, the MFF and PIE modules work synergistically to significantly boost the model’s perception and recall of diverse and low-contrast targets. The CRD then screens and refines these proposals, effectively filtering artifacts and

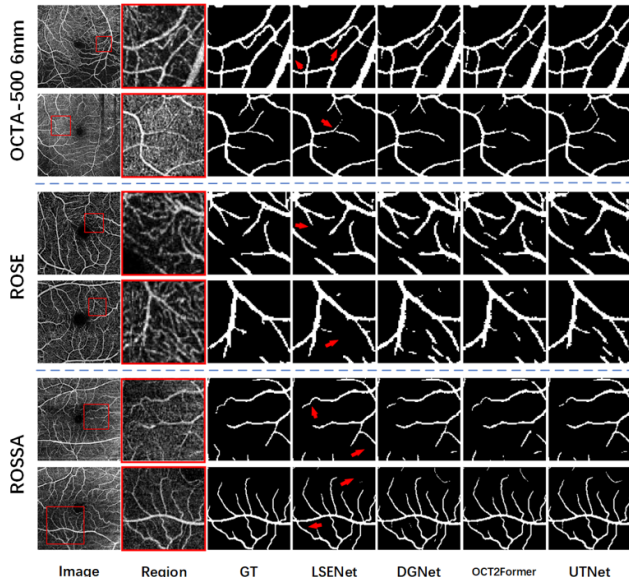


Figure 10. Qualitative comparison on samples from OCTA-500 6mm, ROSE-1, and ROSSA. Columns (from left to right) show: Original Image, Magnified Region, Ground Truth (GT), LSENet (Ours), and competing methods. Red arrows highlight challenging regions where LSENet excels at maintaining vessel connectivity and suppressing false positives.

enforcing vascular connectivity. Each module fulfills a distinct role, enabling LSENet to achieve high performance in complex scenarios.

4.5. Discussion

What roles do the MFF, PIE, and CRD modules play?

The role of PIE is to use local attention to enhance local features. However, we found that the performance of the PIE module was constrained by the encoder’s capabilities. Therefore, we added the MFF module to enable the model to acquire richer information, but this also led to an excess of fragmented targets in our final output. Consequently, we modified the decoder into the CRD, which allows the model to treat the features captured by the preceding modules more cautiously, enhancing the connectivity of the final result.

Why was a more aggressive data augmentation strategy adopted? We increased the rotation range from $\pm 10^\circ$ to $\pm 30^\circ$ to create a more challenging and diverse training distribution, preventing larger models from overfitting early and ensuring a fair comparison of the true learning potential across all architectures. We emphasize that all models, including the traditional CNN-based baselines, were trained from scratch under this identical strategy and monitored until full convergence. By subjecting every model to the same rigorous data regime, we aimed to demonstrate that LSENet’s performance gains stem from its intrinsic architectural capacity to capture robust vessel features rather than from dataset bias. This ensures that the observed SOTA results reflect the models’ actual generalization capabilities in

Table 3. Comparison of parameters, FLOPs, and time for retinal vessel segmentation under 224×224 input conditions.

Model	Params/M	FLOPs/G	Time/ms
UNet	17.27	30.71	4.11
UTNet	57.45	62.23	12.15
SwinUNet	27.14	5.90	11.19
OCT2Former	7.35	50.07	26.88
FRNet	0.01	18.63	6.92
DGNet	1.04	2.74	20.61
LSENet(Ours)	2.08	55.49	27.19

complex clinical environments.

What are LSENet’s advantages compared to other methods?

Fig. 10 demonstrates that our model effectively handles low-contrast regions and produces segmentation results with superior topological connectivity. Architecturally, LSENet enhances interpretability by utilizing down-sampled raw inputs across layers and a large-receptive-field final convolution to capture critical vascular structures. Furthermore, as shown in Tab. 3, our model achieves an exceptionally compact footprint. With only 2.08M parameters, it is approximately $8\times$ smaller than U-Net (17.3M), $27\times$ smaller than UTNet (57.5M), and $13\times$ smaller than SwinUNet (27.1M). This high parameter efficiency demonstrates that LSENet can achieve state-of-the-art representation power while significantly reducing storage requirements, making it highly suitable for memory-constrained medical imaging environments.

5. Conclusion

This paper presents LSENet, a lightweight architecture designed to tackle low local contrast and vessel discontinuity in OCTA segmentation via MFF, PIE, and CRD modules. Extensive evaluations on three public datasets demonstrate that LSENet achieves state-of-the-art performance with superior topological connectivity and noise robustness. With its parameter efficiency and effective local feature enhancement, LSENet offers a promising solution for automated clinical diagnosis in OCTA analysis.

Acknowledgments

This work was supported by the National Science Foundation of China [U23A20389, 62306095, 82441009, 82441008, 62506101]; the Heilongjiang Natural Science Foundation of China [LH2024F021]; the China Postdoctoral Science Foundation [2024M764190]; the Heilongjiang Postdoctoral Science Foundation [LBH-Z24180]; the Heilongjiang Province Science and Technology Talent Support Program Project [CYQN24030]; the Fundamental Research Funds for the Central Universities [HIT.NSFJG202439, HIT.NSFJG202434].

References

- [1] Guogang Cao, Zeyu Peng, Zhilin Zhou, Yan Wu, Yunqing Zhang, and Rugang Yan. Multi-task octa image segmentation with innovative dimension compression. *Pattern Recognition*, 159:111123, 2025. 2
- [2] Hu Cao, Yueyue Wang, Joy Chen, Dongsheng Jiang, Xiaopeng Zhang, Qi Tian, and Manning Wang. Swin-unet: Unet-like pure transformer for medical image segmentation. In *Computer Vision – ECCV 2022 Workshops*, pages 205–218. Springer Nature Switzerland, 2022. 2, 6
- [3] P. Carpineto, R. Mastropasqua, G. Marchini, L. Toto, M. Di Nicola, and L. Di Antonio. Reproducibility and repeatability of foveal avascular zone measurements in healthy subjects by optical coherence tomography angiography. *Br J Ophthalmol*, 100(5):671–6, 2016. 1, 2
- [4] Xiangxiang Chu, Zhi Tian, Yuqing Wang, Bo Zhang, Haibing Ren, Xiaolin Wei, Huaxia Xia, and Chunhua Shen. Twins: revisiting the design of spatial attention in vision transformers. *Nips '21*, 2021. 2
- [5] Alexey Dosovitskiy, Lucas Beyer, Alexander Kolesnikov, Dirk Weissenborn, Xiaohua Zhai, Thomas Unterthiner, Mostafa Dehghani, Matthias Minderer, Georg Heigold, Sylvain Gelly, Jakob Uszkoreit, and Neil Houlsby. An image is worth 16x16 words: Transformers for image recognition at scale. In *2021 International Conference on Learning Representations (ICLR)*, page arXiv 2010.11929, 2021. 2
- [6] Huazhu Fu, Yanwu Xu, Stephen Lin, Damon Wing Kee Wong, and Jiang Liu. Deepvessel: Retinal vessel segmentation via deep learning and conditional random field. In *Medical Image Computing and Computer-Assisted Intervention – MICCAI 2016*, pages 132–139. Springer International Publishing, 2016. 2
- [7] Yunhe Gao, Mu Zhou, and Dimitris N. Metaxas. Utinet: A hybrid transformer architecture for medical image segmentation. In *Medical Image Computing and Computer Assisted Intervention – MICCAI 2021*, pages 61–71. Springer International Publishing, 2021. 6
- [8] Z. Gu, J. Cheng, H. Fu, K. Zhou, H. Hao, Y. Zhao, T. Zhang, S. Gao, and J. Liu. Ce-net: Context encoder network for 2d medical image segmentation. *IEEE Transactions on Medical Imaging*, 38(10):2281–2292, 2019. 2, 6
- [9] K. Hu, S. Jiang, Y. Zhang, X. Li, and X. Gao. Joint-seg: Treat foveal avascular zone and retinal vessel segmentation in octa images as a joint task. *IEEE Transactions on Instrumentation and Measurement*, 71:1–13, 2022. 2
- [10] Tao Jiang, Ying Li, Yifang Li, Wenyu Xing, Ming Yu, Feng Xie, and Dean Ta. A segmentation knowledge-based global-local attention network for tumor classification in breast ultrasound images. *Pattern Recognition*, 171, 2026. 3
- [11] Qiangguo Jin, Zhaopeng Meng, Tuan D. Pham, Qi Chen, Leyi Wei, and Ran Su. Dunet: A deformable network for retinal vessel segmentation. *Knowledge-Based Systems*, 178: 149–162, 2019. 2
- [12] Amir H. Kashani, Chieh-Li Chen, Jin K. Gahm, Fang Zheng, Grace M. Richter, Philip J. Rosenfeld, Yonggang Shi, and Ruikang K. Wang. Optical coherence tomography angiography: A comprehensive review of current methods and clinical applications. *Progress in Retinal and Eye Research*, 60: 66–100, 2017. 1, 2
- [13] L. Kreitner, J. C. Paetzold, N. Rauch, C. Chen, A. M. Hagag, A. E. Fayed, S. Sivaprasad, S. Rausch, J. Weichsel, B. H. Menze, M. Harders, B. Knier, D. Rueckert, and M. J. Menten. Synthetic optical coherence tomography angiographs for detailed retinal vessel segmentation without human annotations. *IEEE Transactions on Medical Imaging*, 43(6):2061–2073, 2024. 2
- [14] Chetan L Srinidhi, P. Aparna, and Jeny Rajan. Recent advancements in retinal vessel segmentation. *Journal of Medical Systems*, 41(4):70, 2017. 1
- [15] Inês Lafíns, Jay C. Wang, Ying Cui, Raviv Katz, Filippos Vingopoulos, Giovanni Staurengghi, Demetrios G. Vavvas, Joan W. Miller, and John B. Miller. Retinal applications of swept source optical coherence tomography (oct) and optical coherence tomography angiography (octa). *Progress in Retinal and Eye Research*, 84:100951, 2021. 1
- [16] M. Li, Y. Chen, Z. Ji, K. Xie, S. Yuan, Q. Chen, and S. Li. Image projection network: 3d to 2d image segmentation in octa images. *IEEE Transactions on Medical Imaging*, 39(11):3343–3354, 2020. 2
- [17] Mingchao Li, Kun Huang, Qiuzhuo Xu, Jiadong Yang, Yuhan Zhang, Zexuan Ji, Keren Xie, Songtao Yuan, Qinghuai Liu, and Qiang Chen. Octa-500: A retinal dataset for optical coherence tomography angiography study. *Medical Image Analysis*, 93:103092, 2024. 2, 5
- [18] Zhenli Li, Xinpeng Zhang, Meng Zhao, Fan Shi, and Wei Zhou. Direction-guided network for retinal vessel segmentation in octa images. *Biomedical Signal Processing and Control*, 103:107455, 2025. 1, 2, 6
- [19] Chang Liu, Kaoru Hirota, and Yaping Dai. Patch attention convolutional vision transformer for facial expression recognition with occlusion. *Information Sciences*, 619:781–794, 2023. 2
- [20] Jianhua Liu, Dongxin Zhao, Juncai Shen, Peng Geng, Ying Zhang, Jiabin Yang, and Ziqian Zhang. Hrd-net: High resolution segmentation network with adaptive learning ability of retinal vessel features. *Computers in Biology and Medicine*, 173:108295, 2024. 2
- [21] Xiaoming Liu, Di Zhang, Junping Yao, and Jinshan Tang. Transformer and convolutional based dual branch network for retinal vessel segmentation in octa images. *Biomedical Signal Processing and Control*, 83:104604, 2023. 1, 2
- [22] Xinyi Liu, Hailan Shen, Wenyan Zhong, Wanqing Xiong, and Zailiang Chen. Dsd-net: Semi-supervised superficial octa vessel segmentation for false positive reduction. *Pattern Recognition*, 165:111592, 2025. 1, 2
- [23] Z. Liu, Y. Lin, Y. Cao, H. Hu, Y. Wei, Z. Zhang, S. Lin, and B. Guo. Swin transformer: Hierarchical vision transformer using shifted windows. In *2021 IEEE/CVF International Conference on Computer Vision (ICCV)*, pages 9992–10002, 2021. 2
- [24] Y. Ma, H. Hao, J. Xie, H. Fu, J. Zhang, J. Yang, Z. Wang, J. Liu, Y. Zheng, and Y. Zhao. Rose: A retinal oct-angiography vessel segmentation dataset and new model. *IEEE Transactions on Medical Imaging*, 40(3):928–939, 2021. 2, 5

- [25] Lieve Moons and Lies De Groef. Multimodal retinal imaging to detect and understand alzheimer’s and parkinson’s disease. *Current Opinion in Neurobiology*, 72:1–7, 2022. 1
- [26] Lei Mou, Yitian Zhao, Huazhu Fu, Yonghuai Liu, Jun Cheng, Yalin Zheng, Pan Su, Jianlong Yang, Li Chen, Alejandro F. Frangi, Masahiro Akiba, and Jiang Liu. Cs2-net: Deep learning segmentation of curvilinear structures in medical imaging. *Medical Image Analysis*, 67:101874, 2021. 2, 4, 6
- [27] H. Ning, C. Wang, X. Chen, and S. Li. An accurate and efficient neural network for octa vessel segmentation and a new dataset. In *ICASSP 2024 - 2024 IEEE International Conference on Acoustics, Speech and Signal Processing (ICASSP)*, pages 1966–1970, 2024. 1, 2, 5, 6
- [28] R. Peng, H. He, Y. Wei, Y. Wen, and D. Hu. Patch matters: Training-free fine-grained image caption enhancement via local perception. In *2025 IEEE/CVF Conference on Computer Vision and Pattern Recognition (CVPR)*, pages 3963–3973, 2025. 2
- [29] Amar Pujari, Karthika Bhaskaran, Pradeep Sharma, Pallavi Singh, Swati Phuljhele, Rohit Saxena, and Shorya Vardhan Azad. Optical coherence tomography angiography in neuro-ophthalmology: Current clinical role and future perspectives. *Survey of Ophthalmology*, 66(3):471–481, 2021. 1
- [30] Xiongwen Quan, Guangyao Hou, Wenya Yin, and Han Zhang. A multi-modal and multi-stage fusion enhancement network for segmentation based on oct and octa images. *Information Fusion*, 113:102594, 2025. 2
- [31] Hongwei Ren, Yue Zhou, Xiaopeng LIN, Yulong Huang, Haotian FU, Jie Song, and Bojun Cheng. Spikepoint: An efficient point-based spiking neural network for event cameras action recognition. In *The Twelfth International Conference on Learning Representations*, 2024. 2
- [32] Hongwei Ren, Yue Zhou, Jiadong Zhu, Xiaopeng Lin, Haotian Fu, Yulong Huang, Yuetong Fang, Fei Ma, Hao Yu, and Bojun Cheng. Rethinking efficient and effective point-based networks for event camera classification and regression, 2025. 2
- [33] Olaf Ronneberger, Philipp Fischer, and Thomas Brox. U-net: Convolutional networks for biomedical image segmentation. In *Medical Image Computing and Computer-Assisted Intervention – MICCAI 2015*, pages 234–241. Springer International Publishing, 2015. 2, 6
- [34] Danuta M. Sampson, Adam M. Dubis, Fred K. Chen, Robert J. Zawadzki, and David D. Sampson. Towards standardizing retinal optical coherence tomography angiography: a review. *Light: Science Applications*, 11(1):63, 2022. 1, 2
- [35] Hailan Shen, Zheng Tang, Yajing Li, Xuanchu Duan, and Zailiang Chen. Haic-net: Semi-supervised octa vessel segmentation with self-supervised pretext task and dual consistency training. *Pattern Recognition*, 151:110429, 2024. 2
- [36] Y. I. Shin, K. Y. Nam, S. E. Lee, H. B. Lim, M. W. Lee, Y. J. Jo, and J. Y. Kim. Changes in peripapillary microvasculature and retinal thickness in the fellow eyes of patients with unilateral retinal vein occlusion: An octa study. *Invest Ophthalmol Vis Sci*, 60(2):823–829, 2019. 1
- [37] Norihiro Suzuki, Yoshio Hirano, Munenori Yoshida, Taneto Tomiyasu, Akiyoshi Uemura, Tsutomu Yasukawa, and Yuichiro Ogura. Microvascular abnormalities on optical coherence tomography angiography in macular edema associated with branch retinal vein occlusion. *American Journal of Ophthalmology*, 161:126–132.e1, 2016. 1, 2
- [38] Xiao Tan, Xinjian Chen, Qingquan Meng, Fei Shi, Dehui Xiang, Zhongyue Chen, Lingjiao Pan, and Weifang Zhu. Oct2former: A retinal oct-angiography vessel segmentation transformer. *Computer Methods and Programs in Biomedicine*, 233:107454, 2023. 1, 2, 6
- [39] Ashish Vaswani, Noam Shazeer, Niki Parmar, Jakob Uszkoreit, Llion Jones, Aidan N. Gomez, Łukasz Kaiser, and Illia Polosukhin. Attention is all you need. In *Proceedings of the 31st International Conference on Neural Information Processing Systems*, page 6000–6010, Red Hook, NY, USA, 2017. Curran Associates Inc. 2
- [40] C. Wang, H. Ning, X. Chen, and S. Li. Db-unet: Mlp based dual branch unet for accurate vessel segmentation in octa images. In *ICASSP 2023 - 2023 IEEE International Conference on Acoustics, Speech and Signal Processing (ICASSP)*, pages 1–5, 2023. 1, 2
- [41] C. Wang, X. Chen, H. Ning, and S. Li. Sam-octa: A fine-tuning strategy for applying foundation model octa image segmentation tasks. In *ICASSP 2024 - 2024 IEEE International Conference on Acoustics, Speech and Signal Processing (ICASSP)*, pages 1771–1775, 2024. 1, 2
- [42] Huisi Wu, Wei Wang, Jiafu Zhong, Baiying Lei, Zhenkun Wen, and Jing Qin. Scs-net: A scale and context sensitive network for retinal vessel segmentation. *Medical Image Analysis*, 70:102025, 2021. 2
- [43] Yicheng Wu, Yong Xia, Yang Song, Donghao Zhang, Dongnan Liu, Chaoyi Zhang, and Weidong Cai. Vessel-net: Retinal vessel segmentation under multi-path supervision. In *Medical Image Computing and Computer Assisted Intervention – MICCAI 2019*, pages 264–272. Springer International Publishing, 2019. 2, 6
- [44] Yicheng Wu, Yong Xia, Yang Song, Yanning Zhang, and Weidong Cai. Nfn+: A novel network followed network for retinal vessel segmentation. *Neural Networks*, 126:153–162, 2020. 2
- [45] Y. Ye, C. Pan, Y. Wu, S. Wang, and Y. Xia. Mfi-net: Multiscale feature interaction network for retinal vessel segmentation. *IEEE Journal of Biomedical and Health Informatics*, 26(9):4551–4562, 2022. 2
- [46] Y. Yuan, L. Zhang, L. Wang, and H. Huang. Multi-level attention network for retinal vessel segmentation. *IEEE Journal of Biomedical and Health Informatics*, 26(1):312–323, 2022. 2
- [47] W. Zhu, L. Sun, J. Huang, L. Han, and D. Zhang. Dual attention multi-instance deep learning for alzheimer’s disease diagnosis with structural mri. *IEEE Trans Med Imaging*, 40(9):2354–2366, 2021. 3
- [48] Yang Zuo, Chen Pang, Chunyu Hu, Chunmeng Kang, Hongbin Lv, and Lei Lyu. Global partition with local enhancement network for multitask learning of malignant melanoma. *Biomedical Signal Processing and Control*, 106, 2025. 3